Volume 3 | Number 7 | 21 February 2015 | Pages 3153–4068

Journal of Materials Chemistry A

Materials for energy and sustainability

www.rsc.org/MaterialsA

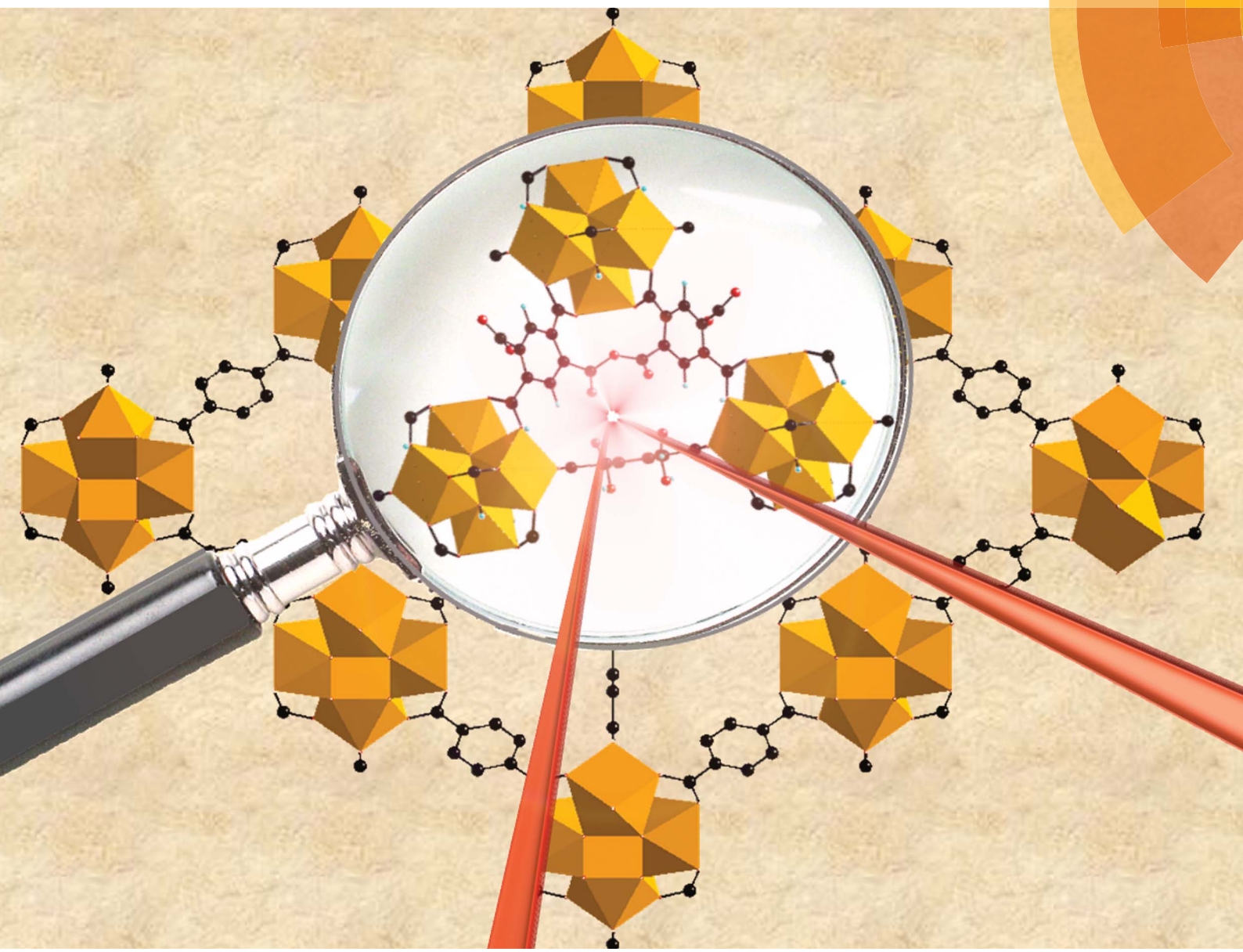

ISSN 2050-7488

ROYAL SOCIETY OF CHEMISTRY

PAPER

Thomas Devic, Guillaume Clet *et al.*

Acid-functionalized UiO-66(Zr) MOFs and their evolution after intra-framework cross-linking: structural features and sorption properties

Journal of Materials Chemistry A

PAPER

Cite this: J. Mater. Chem. A, 2015, 3, 3294

Acid-functionalized UiO-66(Zr) MOFs and their evolution after intra-framework cross-linking: structural features and sorption properties†

Florence Ragon,[a] Betiana Campo,[b] Qingyuan Yang,[cd] Charlotte Martineau,[a] Andrew D. Wiersum,[e] Ana Lago,[a] Vincent Guillerm,[a] Callum Hemsley,[a] Jarrod F. Eubank,[a] Muthusamy Vishnuvarthan,[b] Francis Taulelle,[a] Patricia Horcajada,[a] Alexandre Vimont,[b] Philip L. Llewellyn,[e] Marco Daturi,[b] Sabine Devautour-Vinot,[c] Guillaume Maurin,[c] Christian Serre,[a] Thomas Devic*[a] and Guillaume Clet*[b]

Received 3rd August 2014
Accepted 11th October 2014

DOI: 10.1039/c4ta03992k

www.rsc.org/MaterialsA

The functionalization of metal–organic frameworks (MOFs) with free carboxylic groups is naturally difficult due to their potential coordination with metal ions. The impact of functionalizing the archetypical metal organic framework UiO-66(Zr) with free pending carboxylic groups was thus studied by a multi-technique approach. First, an environmentally friendly water synthesis route was developed to produce UiO-66(Zr)–$(COOH)_x$ ($x = 1, 2$) and the kinetics of crystallization was studied by *in situ* energy dispersive X-ray diffraction. In a second step, the structural features were studied by temperature-dependent X-ray diffractometry and further characterized by density functional theory calculations and solid-state nuclear magnetic resonance spectroscopy. The gas sorption properties, acidity and conductivity features were respectively assessed by gas isotherms and calorimetry, infrared spectroscopy and complex impedance spectroscopy. These data show the noticeable influence of the introduced acidic groups. Finally, it was shown that the thermal treatment of such solids leads to an intra-framework cross-linking associated with the formation of anhydride bridges, as evidenced by FTIR and solid-state NMR, and modelled by DFT simulations. These species have a strong impact on the acidity, but a limited effect on gas sorption properties at room temperature. The reversibility of the carboxylic acids to anhydride transformation was also assessed.

1. Introduction

Unlike many other porous materials, metal organic frameworks (MOFs) can easily be functionalized following different strategies. One convenient approach to fine-tune their properties consists in using a substituted organic ligand. This is an efficient way to directly tune the stability, the physicochemical properties, the catalytic or the sorption-related properties of the material.[1–7] Alternatively, substituted linkers also have potential for subsequent post-synthetic modifications (PSMs).[8] Among the huge number of functional groups which can be introduced, the sulfonic[9–12] or carboxylic[2,12–16] groups are of broad interest. They can be advantageously used to perform acid catalysis, as shown when sulfonic groups were incorporated into MIL-53 and MIL-101 (ref. 9, 11 and 17) (MIL stands for Materials of the Institute Lavoisier), to tune the sorption selectivity for different mixtures, such as favoring the adsorption of CO_2,[18–20] or even to enhance the proton conductivity,[21] as recently highlighted in the case of MIL-53 functionalized solids.[22] On the other hand, carboxylic groups can also be used as reactive groups for PSM, *e.g.* through the formation of amide bonds.[8] Alternatively, carboxylic functional groups may allow the intra-framework cross-linking of the ligands through the formation of anhydride bridges upon dehydration, as observed in the case of MIL-53(Al)–(COOH).[14] If cross-linking is indeed known to improve some properties of materials such as with organic polymers, it is also of interest to determine to what extent it may induce alternative properties in MOFs.[23,24]

[a]Institut Lavoisier, UMR CNRS 8180, Université de Versailles Saint-Quentin-en-Yvelines, 45 avenue des Etats-Unis, 78035 Versailles cedex, France. E-mail: thomas.devic@uvsq.fr

[b]Laboratoire Catalyse et Spectrochimie, ENSICAEN, Université de Caen Basse-Normandie, CNRS, 6 Bd. du Maréchal Juin, 14050 Caen, France. E-mail: guillaume.clet@ensicaen.fr

[c]Institut Charles Gerhardt Montpellier, UMR CNRS 5253, UM2, ENSCM, Place E. Bataillon, 34095 Montpellier cedex 05, France

[d]State Key Laboratory of Organic–Inorganic Composites, Beijing University of Chemical Technology, P. O. Box 100, Beijing 100029, China

[e]Aix-Marseille Univ. – CNRS, Laboratoire MADIREL, UMR 7246, Centre de Saint Jérôme, 13397 Marseille 20, France

† Electronic supplementary information (ESI) available: Details of the synthesis conditions, PXRD, TGA, extended kinetic data of the crystallization, complete description of the modelling methodology, correlation NMR-modelling, and additional gas adsorption data, notably CO and N_2 adsorption at 30 °C. See DOI: 10.1039/c4ta03992k

However, MOFs bearing free sulfonic or carboxylic groups remain rather scarce.[9–14,25] This can be easily explained by the fact that such functions are prone to complex metal cations in the reaction medium to afford new structure types. One way to circumvent this problem relies on post-synthetic modifications;[8,11,20,26] however, this route requires MOFs that are stable to the post-synthetic conditions while a total and homogeneous modification is not assured. Direct synthesis is also possible if the chosen inorganic secondary building unit (SBU) is robust enough to direct the formation of the structure. The Zr_6 unit present in the Zr terephthalate UiO-66(Zr),[27] has proven quite stable and offers potential as such an SBU; in fact, a wide range of polar/non-polar functional groups have already been introduced in analogous structures utilizing this same SBU,[3,10,12,28–32] whilst maintaining in most cases the significant thermal and/or chemical stability of the parent structure.[27,31,33–39] Though the non-functionalized UiO-66(Zr) shows promising adsorption and catalytic properties;[40–44] experimental and computational investigations reveal that the UiO-66(Zr)–(COOH) material presents a higher CO_2/CH_4 selectivity.[12,19] This trend is even more pronounced when a second acidic function was substituted on the organic linker, the resultant UiO-66(Zr)–$(COOH)_2$ outperforming the pristine material for the selective capture of CO_2 from different mixtures whilst maintaining a good water stability.[32,45]

We report here on the in-depth study of the synthesis, structural and sorption properties and thermal behaviour of UiO-66 solids functionalized with carboxylic acid substituents. Especially, whilst most Zr-based MOFs are prepared in toxic solvents (mostly *N*,*N*′-dimethylformamide, DMF), a more environmentally friendly water synthesis route was developed. In order to get a deeper insight into the formation mechanism and to anticipate future possible upscaling, their crystallization kinetics were also studied by time-resolved, energy-dispersive X-ray diffraction (EDXRD). Using a multi-technique approach, combining temperature dependent XRD, thermogravimetric analysis (TGA) together with solid-state nuclear magnetic resonance (NMR), Fourier transform infrared (FTIR) spectroscopy and density functional theory (DFT) calculations, we also evidenced that such solids experience, upon heating, a reversible cross-linking of the ligands[23,24] through the formation of anhydride bridges within the pores. The effect of such a phenomenon on the porosity, acidity and conductivity of the resulting solids was then assessed by adsorption measurements, FTIR and Complex Impedance Spectroscopy (CIS), respectively.

2. Experimental section

2.1 Synthesis

2.1.1 High throughput (HT) synthesis. The HT screening was performed using a stainless steel multiclave reactor block with 24 cavities containing Teflon lined vessels of 2 mL developed by Stock.[46] This reactor was used to study the influence of two different parameters on the formation of crystallized phases, namely the pH and the ligand to cation ratio. The proper amount of ligand either 1,2,4-benzenetricarboxylic acid (H_3BTC) or 1,2,4,5-benzenetetracarboxylic acid (H_4BTeC), (Scheme 1) was first introduced in the reactor, followed by the H_2O–HCl (37%) mixture (volume = 1 mL) and finally $ZrCl_4$ (see ESI, Table S1†). The reaction mixtures were stirred for 5 min, and the sealed multiclave was placed in an oven at 100 °C for 72 hours. After cooling to room temperature, the reaction vessels were filtered, dried in air, and directly examined by HT powder X-ray diffraction (PXRD).

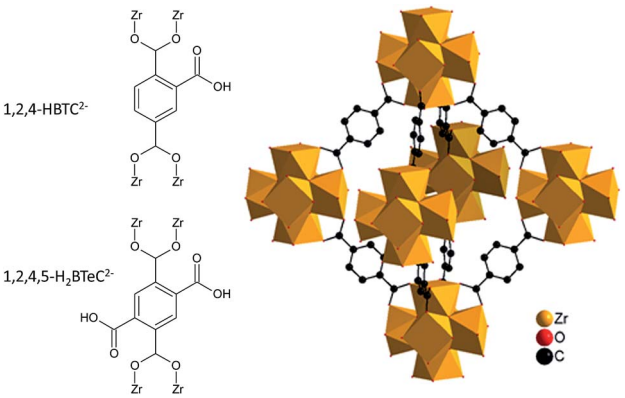

Scheme 1 (Left) Polycarboxylate ligands used in the present study; (Right) view of the parent structure, UiO-66 (octahedral cage).

2.1.2 Optimized synthesis. Both solids (UiO-66(Zr)–(COOH) and UiO-66(Zr)–$(COOH)_2$) were synthesized following the same procedure using a 50 mL round-bottom flask route (see ESI, Table S2†).

In a round-bottom flask equipped with a reflux condenser and a magnetic stirrer, 1.1 g (5 mmol) of H_3BTC (Aldrich, >97%) or 1.3 g (5 mmol) of H_4BTeC (Aldrich, >97%) and 1.2 g (5 mmol) of $ZrCl_4$ (Aldrich, 98%) were dispersed in 25 mL of distilled water (1.4 mol) at room temperature under stirring and then heated under reflux under air for 24 hours. The resulting white gel was filtered off and washed with distilled water at room temperature. The solid was then dispersed in distilled water (~10 mL per 1 g of product) and heated under reflux for 16 hours. The solid was then recovered by filtration, washed with water and dried at 30 °C under vacuum yielding ~2 g of a white powder.

2.2 *In situ* crystallization studies

The crystallization studies were performed in borosilicate Schott DURAN® culture tubes of 12 mm diameter and 100 mm length sealed with screw caps. A reaction volume of around 2 mL and a zirconium concentration of 0.2 M were used (see ESI, Table S3† for details). The starting reagents ($ZrCl_4$ and either H_3BTC or H_4BTeC) were dispersed in distilled water, and the clear solutions were heated at the desired reaction temperature (temperature range: 100–150 °C) using a conventional oven; the temperature was electronically controlled to ±2 K (set up developed by Bensch *et al.*[47]). Reaction mixtures were rapidly stirred during data collection to ensure that solid material remains in the X-ray beam during the whole measurement.

2.2.1 High throughput X-ray powder diffraction data. High throughput X-ray powder diffraction data were collected with a

Bruker D8-Advance diffractometer using CuK_α radiation (λ = 1.54059 Å). The diffractometer is equipped with an x, y sample stage allowing the automatic analysis of the 24 samples issued from the HT synthesis.

2.2.2 Powder X-ray diffraction data (PXRD). Powder X-ray diffraction data (PXRD) were recorded using a conventional high resolution (θ–2θ) Siemens D5000 diffractometer at Cu Kα radiation (λ = 1.54059 Å). DICVOL06 (ref. 48) was used for pattern indexing; the cell refinements were carried out by structureless whole pattern profile refinement using the FULL-PROF software and its graphical interface WINPLOTR.[49]

2.2.3 X-ray thermodiffractometry. X-ray thermodiffractometry was performed with a Siemens D-5000 diffractometer in the θ–θ mode using Co Kα radiation (λ = 1.79 Å) and equipped with in an Anton-Paar chamber. Measurements were performed between 20 and 400 °C with a 10 °C step.

2.3 EDXRD

Product formation was studied by *in situ* EDXRD on the Beamline F3 of the HASYLAB facility (DESY, Hamburg, Germany). This beamline receives white synchrotron radiation with energy 13.5–65 keV and the incident X-ray beam is collimated at 20 × 20 mm^2. Scattered X-rays were detected using a liquid nitrogen cooled solid-state germanium detector positioned at around 2.92° and data accumulated at 30, 60 or 120 s intervals. From the collected EDXRD spectra, the extent of crystallization (α) was extracted by integration of the most intense diffraction peak, namely the (111) Bragg peak for both UiO-66(Zr)–(COOH) and UiO-66(Zr)–$(COOH)_2$ solids. All integrated intensities were normalized by the zirconium fluorescence to take into account the drop of the beam as a function of time and scaled from zero at the beginning of the reaction to unity at the end. These Bragg peak integrations were performed using the software "calf3" (software offered and available for free at beamline F3, private copy by A. Rothkirch/DESY). The crystallization time t_f corresponds to the time when no increase of peak intensity is observed, characterized by the presence of a plateau on the crystallization curve. The induction period t_0 is the time required to detect any crystallinity (normalized peak intensity >5%).

2.4 TGA

TGA curves were recorded on a STA6000 simultaneous thermal analyzer from Perkin-Elmer, under an O_2 atmosphere (20 mL min^{-1}) between room temperature and 600 °C with a heating rate of 2 °C min^{-1}.

2.5 N_2 sorption measurements (−196 °C)

Experiments were performed on a Micromeritics ASAP-2010 apparatus using nitrogen as the probe gas. The UiO-66(Zr)–$(COOH)_x$ solids (50–100 mg) were outgassed at various temperatures ranging from 30 to 200 °C under vacuum for 12 to 24 hours prior to measurement.

2.6 IR spectroscopy

Solid samples were usually analyzed as self-supported wafers (*ca.* 15 mg). In some cases, the solid was deposited on a silicon wafer after dilution in ethanol. The mixture was then dried in air. The wafers were finally placed in an IR quartz cell equipped with KBr windows. The cell was connected to a vacuum line for evacuation, calcination and introduction of known doses of vapours (H_2O and CD_3CN). The compounds were activated in vacuum from room temperature (R.T.; *ca.* 20 °C) to 300 °C, with a dwell of 30 minutes at each temperature chosen (one spectrum every 50 °C). Transmission spectra were recorded in the 500–5600 cm^{-1} range at 4 cm^{-1} resolution on a Nicolet Nexus spectrometer equipped with an extended KBr beam splitting device and a mercury cadmium telluride (MCT) cryo-detector. The spectra were normalized for a 10 mg pellet.

The stability of the anhydrides was tested by leaving the sample, after heating at 200 °C, under 9.3 mbar H_2O for several hours at R.T. For acidity measurements, 26.7 mbar CD_3CN was introduced at R.T. on the solid after heating at various temperatures.

2.7 Solid-state NMR

The ^{13}C cross-polarization under magic-angle spinning (CP-MAS) NMR spectra were recorded on an Avance Bruker 500 NMR spectrometer (B_0 = 11.7 T, corresponding to Larmor frequencies of 500.1 and 125.7 MHz for ^1H and ^{13}C, respectively). The samples were packed on 4 mm outer diameter rotors, and spun at 10 kHz. The initial ^1H 90° pulse length was 3 μs, the contact time was 5 ms, and radiofrequency (RF) fields of 60 and 50 kHz were applied on ^1H and ^{13}C, respectively, during the polarization transfer. ^1H step small-phase incremental alternation (SPINAL-64)[50] decoupling was applied during the signal acquisition (~70 kHz RF field). The recycle delay was 3 s, and about 1000 transients were accumulated for each sample. The ^{13}C chemical shifts were referenced to TMS. The spectra were analyzed using the DMfit software.[51] To study the anhydride formation, the solids were packed in a rotor, put in an oven under 5 mbar vacuum for an hour in temperatures ranging from 25 to 150 °C. After heating, the rotors were rapidly closed to avoid contact with air and moisture. The NMR measurements were then carried out at room temperature. It must be noted that the results arising from these experiments could not be used directly for quantitative information, as the ^{13}C NMR spectra were recorded with a CPMAS sequence for sensitivity purpose.

2.8 Modelling of the structures

The structure of the UiO-66(Zr)–$(COOH)_2$ was previously successfully modelled using a ligand replacement strategy applied to the crystal structure of the parent UiO-66(Zr) followed by a geometry optimization protocol combining force-field based and quantum calculations where both cell parameters and atomic positions were allowed to fully relax.[32] Starting with this crystal structure, the model of the anhydride form was further constructed by connecting two neighbouring

carboxylate groups *via* the deletion of one –OH group from one ligand and one hydrogen atom from the other. The so-obtained model was then geometry optimized by the same computational strategy mentioned above (see ESI† for more details).

The theoretical accessible surface area and pore volume for each structure were further calculated using the geometric[52] and thermodynamic[53] methods respectively (see ESI†). The calculations of the ^{13}C isotropic chemical shifts were performed with the CASTEP density-functional-theory (DFT)-based code. The projector augmented waves (PAW)[54] and gauge included projector augmented waves (GIPAW)[55] algorithms were considered. The Perdew–Burke–Ernzerhof (PBE) functional[56] was used in the generalized gradient approximation (GGA) for the exchange correlation energy and the core–valence interactions were described by ultrasoft pseudopotentials.[57]

2.9 Gas adsorption and calorimetry

To follow the influence of outgassing temperature on the gas uptakes in the adsorption isotherms, a recently developed 'high throughput' adsorption apparatus with six adsorption stations was used.[58] Here, samples from the same batch were placed into different adsorption stations and outgassed under vacuum to 30, 50, 75, 100, 150 and 200 °C respectively. The adsorption of methane and carbon dioxide was then performed at 30 °C and up to 30 bar.

The adsorption energies were obtained for samples outgassed under vacuum to 30 °C and 150 °C for nitrogen, methane, carbon monoxide and carbon dioxide. These enthalpies were measured experimentally at 30 °C and up to 40 bar using a Tian–Calvet type microcalorimeter coupled to an in-house manometric gas dosing system.[59] This apparatus allows the simultaneous measurement of the adsorption isotherm and the corresponding differential enthalpies. Gas is introduced into the system using a step-by-step method and each dose is allowed to stabilize in a reference volume before being brought into contact with the adsorbent, located in the microcalorimeter. The introduction of the adsorbate to the sample is accompanied by an exothermic thermal signal, measured by the thermopiles of the microcalorimeter. The peak in the calorimetric signal is integrated over time to give the total energy released during that adsorption step.

2.10 Conductivity measurements

The proton conductivity was measured by ac impedance spectroscopy, using a Novocontrol dielectric alpha analyzer, in the 10^{-2} to 10^{4} Hz frequency range. The conductivity of the solids was derived from the dc plateau deduced from the plot of the ac conductivity with respect to the frequency. Measurements were performed at 25 °C, using the Quatro Novocontrol system, *via* nitrogen flux. To avoid the use of mechanical constraint, conductivity experiments were not carried out on pellets prepared from compressed powder. Rather, we employed a specific cell similar to the one generally used for liquids. About 100 mg of the powder sample was poured on the lower electrode of the cell, and then very gently pressed by the upper metallic electrode. The activated solids were hydrated by maintaining the cell in contact with a water saturated atmosphere for 24 hours at room temperature. The cell was then transferred into the cryostat of the impedancemeter and the solid was *in situ* treated at 25 °C under dried nitrogen, for 30 min, before conductivity measurements.

3. Results and discussion

3.1 Synthesis and *in situ* crystallization studies

3.1.1 High throughput and kinetic studies. Zr carboxylate-based MOFs are traditionally obtained under solvothermal conditions from a solution of $ZrCl_4$ (or $ZrOCl_2 \cdot xH_2O$) and polycarboxylic acids in a polar solvent (DMF, *N*,*N*′-diethylformamide (DEF) or dimethylacetamide (DMA)), sometimes in the presence of acidic modulators (*e.g.* hydrochloric or monocarboxylic acids) to achieve a good crystallinity.[44,60–63] So far, only minor amounts of water (coming from the reactants or additives) were introduced in the reaction mixtures, acting more as a reactant or a modulator rather than a solvent. Nevertheless, as the Zr_6 units are robust and able to be formed in water,[64,65] UiO-66(Zr) type solids are likely to be synthesized in pure water, providing that the organic linker is soluble enough (*e.g.* 2-nitroterephthalic acid[66]). Indeed, using polar terephthalic derivatives (*i.e.* 1,2,4-benzenetricarboxylic acid and 1,2,4,5-benzenetetracarboxylic acid) and $ZrCl_4$ in water under hydrothermal conditions, we were able to produce UiO-66 derivatives (UiO-66(Zr)–(COOH) and UiO-66(Zr)–$(COOH)_2$, respectively), as confirmed by PXRD analysis (see ESI, Fig. S1 and S2†).

In a first step, a high-throughput (HT) methodology[46] was employed to study the influence of two experimental parameters, namely the ligand to metal ratio (L : M) and the HCl content on the reaction product, while the temperature was kept constant (100 °C). Both parameters were indeed found to notably affect the crystallinity of UiO-66 derivatives prepared in DMF.[61,66] The results are summarized in Fig. 1.

For any experimental conditions, only UiO-66 type materials were observed (see as an example Fig. 2), confirming the robustness of this structure type even in the presence of additional complexing functional groups. While the L : M ratio seemed to have a minor effect on the crystallinity, addition of a large excess of HCl prevented the formation of the solid, the

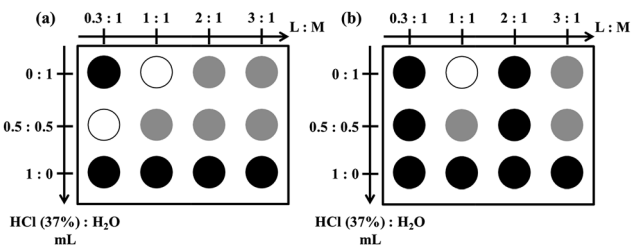

Fig. 1 HT investigation of the influence of L : M ratio and HCl (37 wt% or 12 M)–H_2O ratio on the product formation in the system (a) $ZrCl_4$/BTC and (b) $ZrCl_4$/BTeC. Experiments were carried out in a closed vessel at 100 °C for 72 hours. Black: amorphous solid or recrystallized ligand; grey: poorly-crystallized UiO-66 type solid; white: well-crystallized UiO-66 type solid.

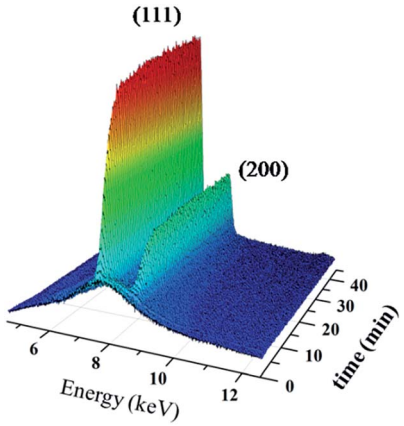

Fig. 2 Time-resolved *in situ* EDXRD data of the hydrothermal synthesis of the UiO-66(Zr)–(COOH) solid synthesized at 150 °C with 7.5 eq. HCl/Zr. The two main Bragg peaks (111) and (200) are shown.

extreme acidity probably limiting the deprotonation of the linker.

The crystallization kinetics of both UiO-66(Zr)–(COOH) and UiO-66(Zr)–$(COOH)_2$ were further investigated by means of time-resolved EDXRD. For the sake of comparison, the experimental conditions (HCl/Zr ratio) previously used for the studies of UiO-66(Zr) derivatives were kept.[61,66] The crystallization reactions were carried out from 110 to 150 °C to not only observe the temperature effect but also to assess the characteristic parameters of the reactions (*e.g.* activation energy). As an example, the results of the crystallization process at 150 °C for UiO-66(Zr)–(COOH) are shown in Fig. 2 and 3 shows the normalized crystallization curves produced for both compounds by the integration of the (111) Bragg peaks at different temperatures.

First, whatever the ligand (H_3BTC or H_4BTeC) and the temperature (110, 120, 130, 140, and 150 °C) considered, no intermediate crystalline phase was observed prior to the formation of UiO-66, once again confirming the robustness of such a structure type. At 110 °C, the reactions are completed within a few hours, whereas higher temperatures (>130 °C) led to very short crystallization times t_f, shorter than 30 minutes (see ESI, Table S5†), as already observed for UiO-66 analogues prepared in DMF.[61,66] If one takes into account the full shape of the crystallization curve, a striking difference emerges between UiO-66(Zr)–$(COOH)_2$ and UiO-66(Zr)–(COOH). Whilst for the first one, the crystallization starts as soon as the solution is heated, for the second one a first step of induction, with no crystallization, is observed (Fig. 3 and S5†). This induction time t_0 (see ESI, Table S5†) decreases with increasing temperature. The reason of such a discrepancy remains unclear, and seems to have no direct connection with solubility issues, H_3BTC being more soluble than H_4BTeC in water.[67]

In order to extract the kinetic information from the EDXRD data, the crystallization curves were fitted using two models. The first one is the Avrami–Erofe'ev model, eqn (1), which relates the extent of crystallization α to the reaction time t and the induction time t_0 (eqn (1)), allowing the extraction of the

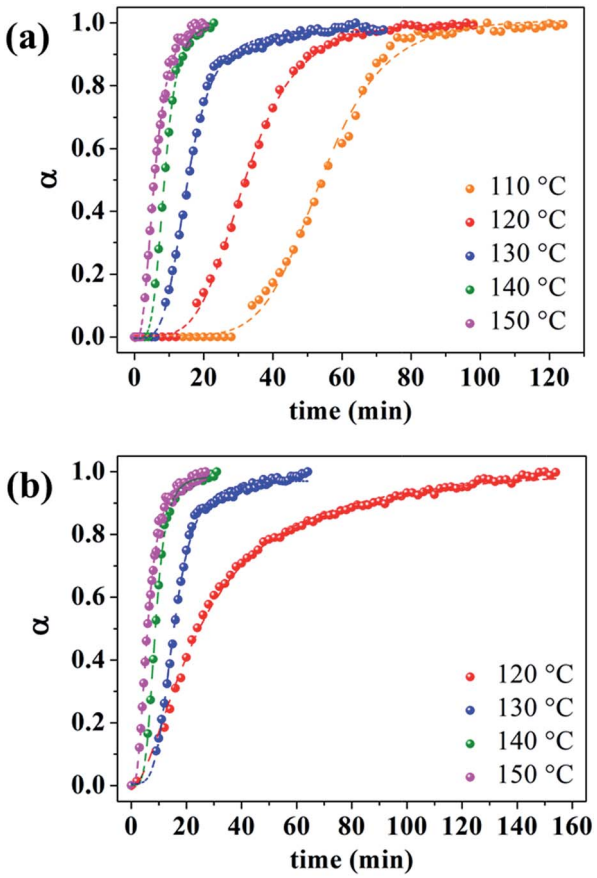

Fig. 3 Plots of the extent of crystallization (α) against time obtained by integration of the (111) Bragg peak of the (a) UiO-66(Zr)–(COOH) and (b) UiO-66(Zr)–$(COOH)_2$ synthesized at different temperatures using $ZrCl_4$ in the presence of 7.5 HCl/Zr. The crystallization curves were fitted using sigmoidal functions for clarity.

Avrami exponent n_{SH} and the rate constant k_{SH}.[68,69] The second one is the Gualtieri model (2),[70] which considers nucleation and growth as distinct processes, where a ($= 1/k_n$) and b are constants related to the nucleation, while k_g and n are the rate constant of the crystal growth and the dimension of the growth ($n = 3$ for a cubic symmetry), respectively.

$$\alpha = 1 - \exp(-k_{SH}(t - t_0))^{n_{SH}} \quad (1)$$

$$\alpha = \frac{1}{1 + \exp^{-(t-a)/b}}\left[1 - \exp^{-(k_g \times t)^n}\right] \quad (2)$$

Concerning the first model, plotting $\ln(-\ln(1 - \alpha))$ *versus* $\ln(t - t_0)$ (see ESI, Fig. S6† for the Sharp–Hancock[71] linearization) leads to two linear regions with different slopes. This observation indicates that two dominating mechanisms take place during the crystallization, as already reported for few other solids (including MOFs).[72–74] Thus, this non-unique linearity precludes the extraction of meaningful n_{SH} values. Using the Gualtieri model eqn (2), we extracted both the nucleation (k_n) and growth (k_g) rates (see ESI, Table S6†). In all cases, $k_g > k_n$ indicates that the nucleation process is rate-limiting, as already

observed for the non-functionalized UiO-66 solid.[61] Finally, for both materials and processes (nucleation and growth), the activation energies (E_a) were extracted (see ESI, Fig. S9†) using the Arrhenius eqn (3).

$$k = A \exp(-E_a/RT) \quad (3)$$

These values are summarized in Table 1. Although it is not obvious to relate these data to the physico-chemical parameters, one can note that these values are on the whole similar to those measured for other MOF systems, belonging or not to the UiO-66 series.[61,66,74,75]

From these experiments, it was obvious that both UiO-66(Zr)–(COOH) and UiO-66(Zr)–$(COOH)_2$ could be prepared under reflux conditions ($T = 100$ °C) at a reasonable time (~1 day). Using a round-bottom flask in a room-pressure setup, their synthesis procedures were optimised, to finally produce both UiO-66(Zr)–(COOH) and UiO-66(Zr)–$(COOH)_2$, under reflux in water in only 24 h (see the Experimental section for details). These final experimental conditions (water, 100 °C) appear 'greener' and cheaper than the one initially reported by Biswas *et al.*[12] for the preparation of UiO-66(Zr)–(COOH) (DMF, 150 °C) and moreover, are easily scalable, as recently exemplified by the preparation of UiO-66(Zr)–$(COOH)_2$ at the 40 g scale.[32]

3.1.2 Thermal analysis. The thermal behaviour of the title solids was first analyzed by thermogravimetric analyses as shown in Fig. S3.† Both solids present a similar behaviour with a first marked weight loss below 100 °C, attributed to the free water departure, followed by a slightly decreasing plateau between 100 and 300 °C and, finally, another pronounced weight loss at higher temperature (>300 °C) associated with the full degradation of the linker. Weight losses matched with the chemical formula $Zr_6O_4(OH)_4(O_2C–C_6H_3–CO_2–CO_2H)_6 \cdot xH_2O$ ($x \sim 14$) and $Zr_6O_4(OH)_4(O_2C–C_6H_2–CO_2–(CO_2H)_2)_6 \cdot xH_2O$ ($x \sim 17$) for UiO-66(Zr)–(COOH) and UiO-66(Zr)–$(COOH)_2$, respectively. Nevertheless, one cannot fully exclude a slight sub-stoichiometry of the ligands, as already detected for UiO-66(Zr).[41,76] Chemical analysis (see ESI, Table S4†) indeed suggests this might be the case for UiO-66(Zr)–(COOH).

Temperature dependent PXRD patterns are shown in Fig. 4 and evidence that both structures remain intact up to 200 and 250 °C for UiO-66(Zr)–(COOH) and UiO-66(Zr)–$(COOH)_2$, respectively. Such temperatures are significantly lower than the ones observed for other UiO-66 type solids. Although this may indicate a degradation of the solids, the TGA did not show any significant weight loss in this temperature range. Alternatively, a loss of long-distance order without any major chemical degradation could induce such changes of the PXRD patterns.

Table 1 Activation energy of UiO-66(Zr)–(COOH) and UiO-66(Zr)–$(COOH)_2$ deduced from Arrhenius plots

Solid	E_{an} (kJ mol^{-1})	E_{ag} (kJ mol^{-1})
UiO-66(Zr)–(COOH)	86(3)	49(12)
UiO-66(Zr)–$(COOH)_2$	85(6)	56(24)

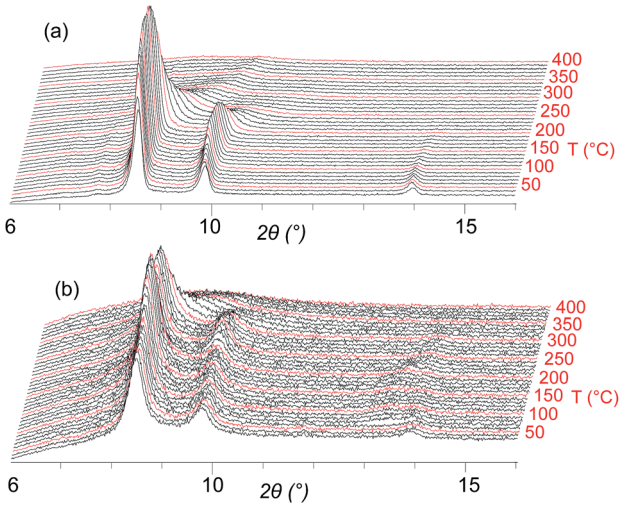

Fig. 4 X-ray thermodiffractometry under air ($\lambda_{Co} \sim 1.79$ Å) of (a) UiO-66(Zr)–(COOH) and (b) UiO-66(Zr)–$(COOH)_2$. Each red line corresponds to a 50 °C stage.

In order to shed light onto this peculiar behaviour, temperature dependent spectroscopic studies were performed, whose results are detailed in the next section.

3.2 Development of cross-linking species

3.2.1 Formation of anhydrides upon heating. The thermal behaviour of the title solids was studied by FTIR under vacuum. The characteristic peaks obtained during the heat treatment of the UiO-66(Zr)–(COOH) are described below. Very similar results were obtained for UiO-66(Zr)–$(COOH)_2$.

FTIR spectra of the solids (Fig. 5) show the usual bands for MOF carboxylates, notably bands around 1600–1400 cm^{-1} due to –COO groups linked to the metal centres.[41] The FTIR spectrum of the as-synthesized UiO-66(Zr)–(COOH) under vacuum shows a broad band around 1712 cm^{-1}. This band is characteristic of a free carboxylic group, *i.e.* the carboxylic side-group of the ligand or unreacted ligand molecules. This band first sharply decreases upon mild heating and, around 100 °C, splits into two bands at 1690 and 1743 cm^{-1}. Comparable splits are observed in the case of acid hydrates.[77] The position of the band at 1690 cm^{-1} is in agreement with the carboxylic side-group assignment. The band at 1743 cm^{-1} decreases upon heating and completely disappears around 250 °C. This might be due to perturbed ν(C=O) vibration. In contrast, above 100 °C, new bands are observed at 1787, 1797 (shoulder), 1852 and 1866 cm^{-1} and also at 896 and 932 cm^{-1}. These bands are characteristic of strained anhydride species,[14,78] and develop when the temperature increases. It may be noteworthy to mention that these bands develop at much lower temperature than on MIL-53(Al)–(COOH).[14] These species persist upon cooling to room temperature under vacuum. Similar bands were observed with UiO-66(Zr)–$(COOH)_2$, except for slight changes in the position or relative band intensities of the anhydride bands: bands were indeed observed at 1786, 1804 and 1861 cm^{-1} and at 902 and 1019 cm^{-1}.

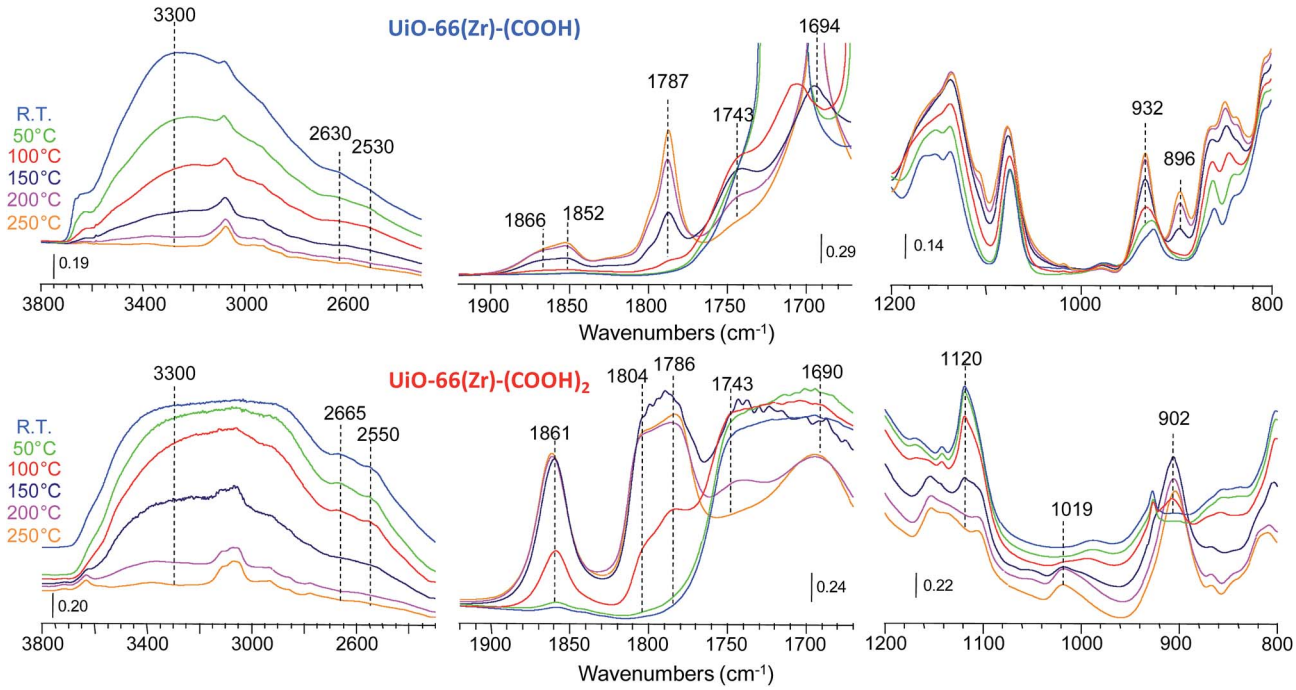

Fig. 5 FTIR spectra upon heat treatment of UiO-66(Zr)–(COOH) (top) and UiO-66(Zr)–$(COOH)_2$ (bottom).

For both solids, a broad band is observed in the OH region, at around 3300 cm^{-1}, indicating large perturbations by H-bonding as usually observed for the OH groups of carboxylic acids. Interactions with adsorbed water may also participate in the broadening of this band. This band is accompanied by others at around 2640 and 2540 cm^{-1}, which are characteristic of strong hydrogen bonds between facing carboxylic acid groups.[77] These bands decrease upon heating and disappear at around 250 °C at the same time as the one at 1743 cm^{-1}. At this stage, the anhydride bands did not increase anymore. It is thus likely that the proximity of adjacent COOH groups first gives rise to O–H···O hydrogen bonds which vanish when anhydride bridges appear.

The development of anhydride species has been quantified on both UiO-66(Zr)–$(COOH)_x$ materials. Their amount sharply increases above 50 °C and then reaches a plateau around 200 °C (Fig. 6). Noteworthily, the amount of anhydrides on UiO-66(Zr)–$(COOH)_2$ is *ca.* 3.5 times larger than on UiO-66(Zr)–(COOH). This might be in agreement with the simple probability of finding two carboxylic groups in front of each other across the pore. This should be four times larger on UiO-66(Zr)–$(COOH)_2$ than on UiO-66(Zr)–(COOH). This suggests that anhydrides are formed as long as the free carboxylic groups are in close proximity.

The evolution of the anhydride formation can be compared with the decreasing intensity of bands due to the carboxylic acids. Fig. 6b shows, as expected, that for both solids, the development of the anhydrides was accompanied by a decrease of the bands due to carboxylic groups. However, these two parameters cannot be quantitatively and directly correlated due to (i) band shifts in these regions and (ii) the fact that only a part of the carboxylic group is initially interacting with a second carboxylic group and can thus further dehydrate.

The development of the anhydride bands has been compared to the evolution of the bands related to hydroxyl groups. No clear correlation can be observed between the anhydride bands and the band at ~3300 cm^{-1}. By contrast, Fig. 7 shows that for both solids, the amount of anhydrides formed is directly correlated with the decrease of the amount of hydroxyl groups involved in short hydrogen-bonds (bands around 2640 and 2540 cm^{-1}). This indicates that only carboxylic groups in close interaction will be able to yield anhydride species. In addition, it is noteworthy that both curves are parallel to each other. This implies that, in this pore configuration, the unavoidable presence of some carboxylic groups close to each other is the only factor that will influence the final formation of anhydrides upon heating.

The ^{13}C CPMAS NMR spectra of UiO-66(Zr)–$(COOH)_2$ and UiO-66(Zr)–(COOH) after activation at various temperatures are shown in Fig. 8. After activation at 25 °C, both spectra contain two sets of peaks: a first set located in the 170–180 ppm range, which corresponds to the carboxyl carbon atoms and a second set in the 110–140 ppm range, which corresponds to the quaternary and C–H carbon atoms of the $HBTC^{2-}$ and H_2BTeC^{2-} linkers. Based on the line intensity and DFT-calculations of the ^{13}C isotropic chemical shifts, the ^{13}C NMR resonances have previously been assigned to the various carbon atoms in UiO-66(Zr)–$(COOH)_2$.[32] In particular, the line at a lower chemical shift (170 ppm) was assigned to the C–O–Zr carbon atom, whilst the line at a higher chemical shift (176 ppm)

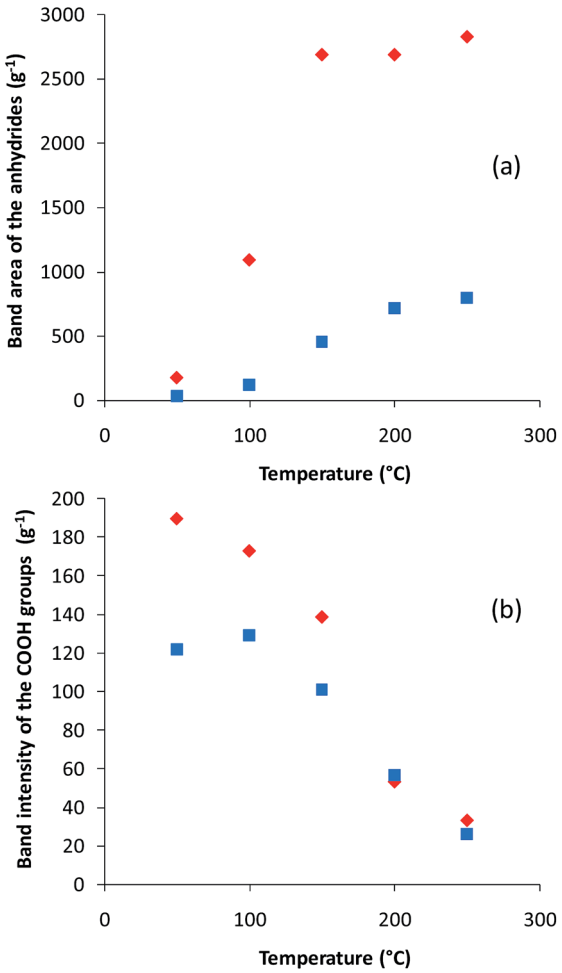

Fig. 6 Comparison of the amount of species observed by FTIR on UiO-66(Zr)–(COOH) (■) and UiO-66(Zr)–$(COOH)_2$ (◆): (a) anhydrides (band at *ca.* 1860 cm^{-1}) and (b) COOH groups (band at 1743 cm^{-1}).

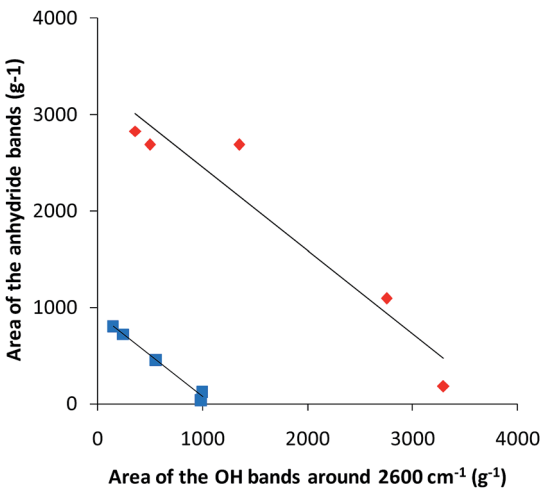

Fig. 7 Role of the strongly hydrogen-bonded OHs on the formation of anhydrides in UiO-66(Zr)–(COOH) (■) and UiO-66(Zr)–$(COOH)_2$ (◆).

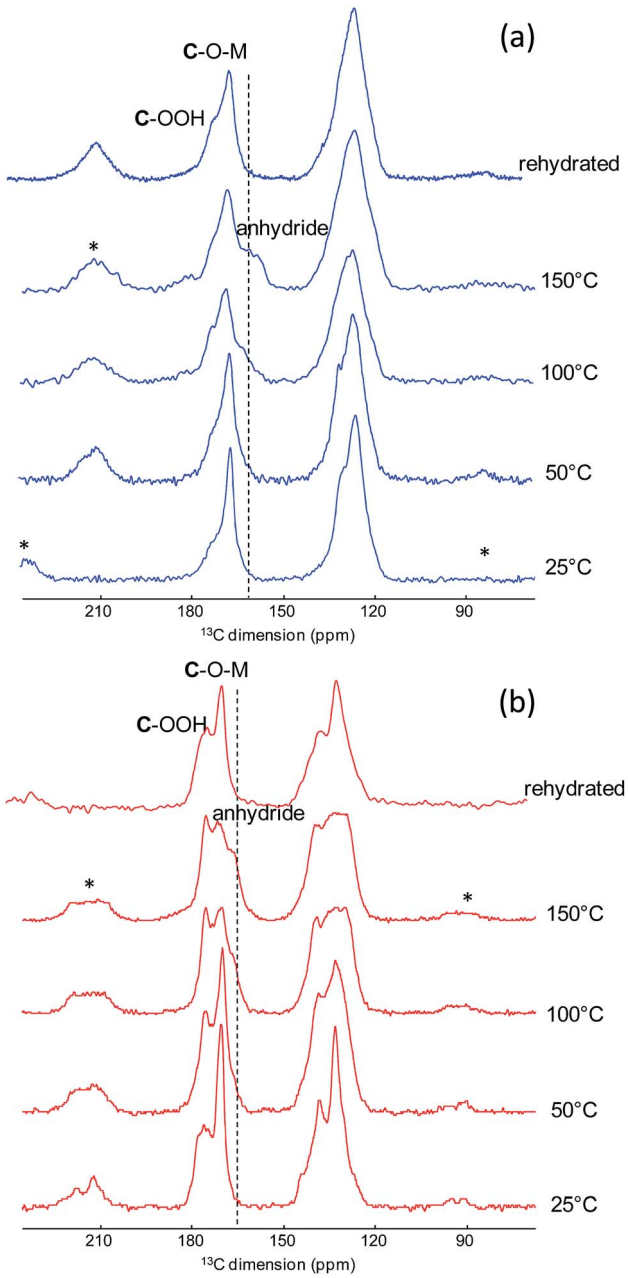

Fig. 8 ^{13}C CPMAS NMR spectra of UiO-66(Zr)–(COOH) (a) and UiO-66(Zr)–$(COOH)_2$ (b) recorded on the sample previously heated at temperatures in the range 25–150 °C. On top are shown the spectra of the rehydrated solids. The stars indicate the spinning sidebands. The dashed lines are merely a guide to the eye.

corresponded to the 'free' carboxyl function from the BTeC linker. A similar line assignment can be made in UiO-66(Zr)–(COOH) (see Fig. 8).

In both solids, a peak appears around 166 ppm upon heating. This chemical shift is close to the one reported for the formation of anhydride in MIL-53–$(COOH)_2$,[14] in agreement with the formation of anhydride bridges by condensation of two neighbouring free carboxyl groups.

NMR analyses indeed confirm the presence of a large amount of anhydride species, which cannot be explained solely

by defective sites (such as intra-molecular ligand dehydration), but more likely by cross-linking anhydrides between two ligands. In order to estimate the geometric feasibility of such cross-linked anhydride species and to confirm NMR assignments, DFT calculations were achieved to propose a plausible structure model of the anhydride structure as the quality of the PXRD pattern prevented any accurate structure determination from diffraction analysis. A model was built starting from the previously modelled structure of UiO-66(Zr)–$(COOH)_2$.[32] The latter was built-up in a cubic unit-cell with the *F*23 space group, in agreement with the experimental data (see ESI†). In the construction of the anhydride form, 32 hydrogen atoms and 16 oxygen atoms (corresponding to 16 H_2O molecules) are removed (per unit-cell), leading to a structure containing 16 –COOH groups (that is, $8H_2BTEC^{2-}$ organic linkers) and 16 –COOCO groups per unit cell. The so-obtained structure was further DFT geometry optimized with a full relaxation of both atomic positions and cell parameters, leading finally to an orthorhombic (but close to cubic) unit-cell. The geometric features of the optimized anhydride structure are compared with the ones previously reported for the modelled UiO-66(Zr)–$(COOH)_2$ in Table 2.

A fragment of such a structure is presented Fig. 9. It shows that the formation of anhydride bridges between neighbouring ligands (angle ligand 1 − Zr_6 − ligand 2 = 60°) is geometrically feasible without any drastic structural distortion.

The above NMR assignments were confirmed by further DFT calculations performed on the anhydride structure. The calculated isotropic ^{13}C shifts indeed agree very well with the experimental values as summarized in Table 3, similarly what has been previously obtained for UiO-66(Zr)–$(COOH)_2$. We further checked that such a correlation was not generated by chance considering for each form of UiO-66(Zr) a structure that was not preliminarily optimized and for which the calculations of the isotropic ^{13}C shifts were repeated. One observes in Fig. S10† that the correlation between experimental and simulated ^{13}C shifts is of much less quality than the one obtained based on the optimized structure. These findings, combined with our previous studies on a series of functionalized UiO-66(Zr),[79] not only allowed us to provide a further validation of the predicted crystal structures for this anhydride form but also for the UiO-66(Zr)–$(COOH)_2$ solid.

3.2.2 Influence of the anhydrides on gas sorption properties. As shown above in Fig. 6, increasing the activation temperature of these solids favours the formation of anhydride species. To follow this effect on the accessible surface area and pore volume, nitrogen adsorption at −196 °C was carried out on the solids after outgassing at different temperatures. The resulting BET (Brunauer–Emmett–Teller) surface areas and pore volumes are shown in Fig. 10 and Table S7,† and can be compared with the theoretical results, extracted from the simulated structures, in Table 2.

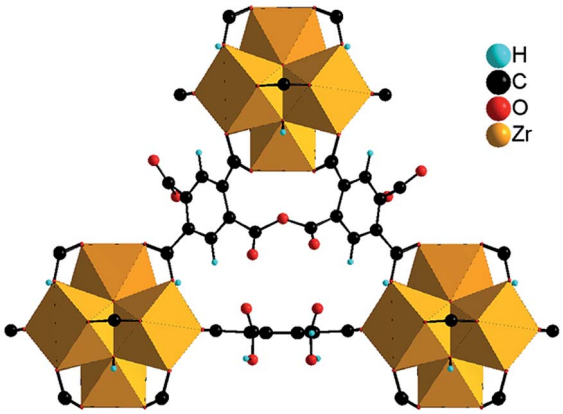

Fig. 9 Simulated structure of the anhydride form of UiO-66(Zr)–$(COOH)_2$: view of an anhydride bridge formed between two adjacent ligands. This figure also highlights the reduction of the size and rigidification of the triangular pore windows upon dehydration.

First, as expected,[19] the presence of bulky COOH groups, induced a decrease in the BET area compared to the parent UiO-66(Zr). The experimental BET areas are slightly higher than the values calculated theoretically in this study (Table 2). On the whole, UiO-66(Zr)–(COOH) shows a lower surface area and UiO-66(Zr)–$(COOH)_2$ a higher surface area than the values reported by Biswas *et al.*[12,31]

As shown in Table 2, the theoretical approach suggests that hardly any change in the accessible surface area and pore volume can be expected on the formation of anhydride species in the two UiO-66(Zr)–$(COOH)_x$ structures. The variation of the experimental BET area as a function of the activation temperature is plotted in Fig. 10a. Similar variations were obtained for the pore volumes (ESI, Table S7†). It can be seen that for both UiO-66(Zr)–$(COOH)_x$ at low temperature (<70 °C), increasing the temperature of activation leads to a slight increase in BET areas and pore volumes. At higher temperature (especially >130 °C),

Table 2 Structural features of the UiO-66(Zr)–$(COOH)_x$ and the anhydride form of UiO-66(Zr)–$(COOH)_2$

	Experimental		Theoretical			
Materials	Possible space group	Lattice param. (Å)	Space group	Lattice param. (Å)	V_{pore} ($cm^3\ g^{-1}$)	a_{acc} ($m^2\ g^{-1}$)
UiO-66(Zr)–(COOH)[a]	*F*23	20.758(1)	*P*1	20.8039	0.31	551
UiO-66(Zr)–$(COOH)_2$[b]	*F*23	20.731(5)	*F*23	20.9674	0.26	428
Anhydride form	Not determined		*F*222	$a = 20.9725$ $b = 20.8143$ $c = 20.8758$	0.29	464

[a] Theoretical data from ref. 19. [b] Theoretical data from ref. 32.

Table 3 Experimental $\delta_{iso,exp}$ (ppm) and DFT-calculated $\delta_{iso,calc}$ (ppm) ^{13}C isotropic chemical shifts of UiO-66(Zr)–$(COOH)_2$ and of the anhydride form (in bold) and the corresponding assignment. As lines 1 and 2 have very close chemical shifts, the assignments of these two lines could be exchanged

Line	$\delta_{iso,exp}$ (±1)	$\delta_{iso,calc}$	Assignment
1	134	133.8	C_{quat}
	135	**136.0**	
2	135	134.1	CH
	139	**142.1**	
3	139	141.7	C–COOH
	139	**140.9**	
4	171	171.3	C–O–Zr
	171	**171.4**	
5	176	174.4	C–OOH
6	**168**	**168.6**	C–O–C

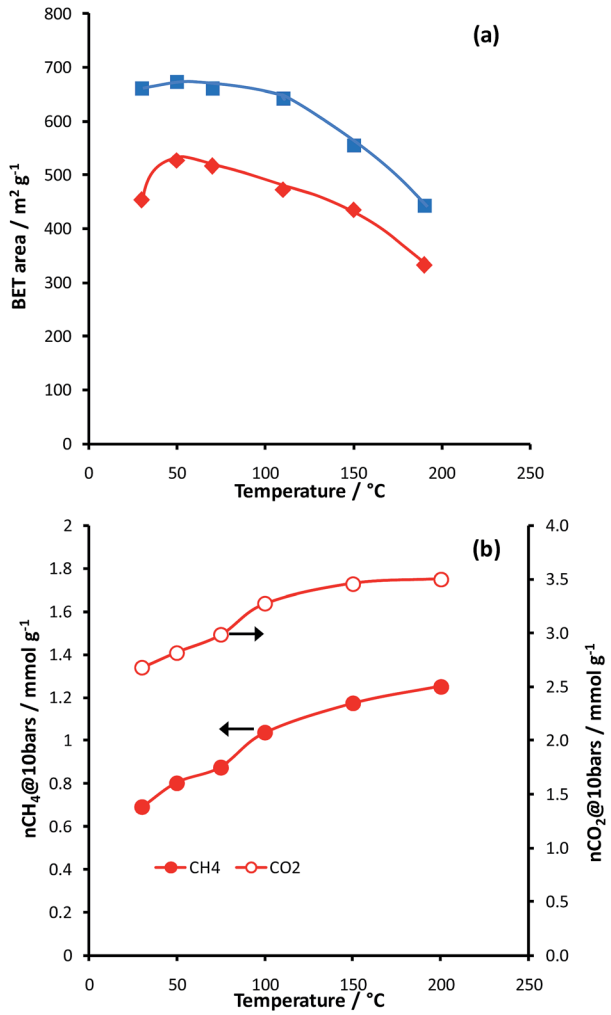

Fig. 10 Effect of outgassing on the adsorption properties. (a) Variation of the BET area for UiO-66(Zr)–(COOH) (■; blue) and UiO-66(Zr)–$(COOH)_2$ (◆; red) from nitrogen sorption at −196 °C, and (b) variation of amounts of CO_2 (○) and CH_4 (●) adsorbed at 10 bars at 30 °C for the UiO-66(Zr)–$(COOH)_2$ solid.

the effect is opposite with a higher activation temperature leading to lower sorption capacities. Below 200 °C, neither XRD, nor TGA nor infrared spectroscopy gave any indication of sample degradation which would explain the porosity decrease. This decrease must then be attributed to other factors. As shown earlier, the amount of anhydride becomes significant at these temperatures. However, from modelling data, the presence of anhydride is expected to modify the surface area and pore volume (see the anhydride form in Table 2) only slightly. Nevertheless, such theoretical calculations only take into account the availability of the pore space, and not its accessibility. At low temperature, when motions are more limited, the formation of anhydride bridges between facing ligands may both decrease the size of the pore apertures (triangular windows) and rigidify the framework (rotation of the phenyl rings is no longer possible); both effects may prevent the efficient adsorption of nitrogen at low temperature (−196 °C) and hence decrease the total sorption capacity, as experimentally observed.

The effect of outgassing temperature and thus anhydride formation has also been studied with respect to the adsorption properties of gases at 30 °C. The uptakes at 10 bar for methane and carbon dioxide adsorbed on UiO-66(Zr)–$(COOH)_2$ are shown as a function of the activation temperature in Fig. 10b (adsorption isotherms are shown in Fig. S12†). In contrast to the variations of surface area measured at −196 °C (Fig. 10a), at 30 °C the amount of gases adsorbed at 10 bar increases with increasing activation temperature.

To gain a deeper insight into the influence of the presence of anhydrides, calorimetry experiments were carried out at 30 °C with methane, carbon dioxide, nitrogen and carbon monoxide with the UiO-66(Zr)–$(COOH)_2$ solid after outgassing to 30 °C and 150 °C. The results obtained with methane and carbon dioxide are given in Fig. 11, and the results with N_2 and CO are provided in the ESI, Fig. S13.†

For both methane and carbon dioxide (the same holds true for nitrogen and carbon monoxide, see ESI†) the difference in activation temperature has no effect on the adsorption enthalpies, associated with little changes in the pore size or shape. In the case of CO_2 only, a slight increase in overall enthalpies of adsorption is observed with increased coverage on the solid outgassed at 150 °C while its initial enthalpy does not change.

All these results indicate that the presence of anhydride species does not induce any detrimental effect on the gas uptake at 30 °C, with no significant change of enthalpy values. Furthermore, this confirms that the loss of capacity, observed with nitrogen at −196 °C after activation above 100 °C, is not related to the degradation of the framework. Nevertheless, the differences obtained on the anhydride form between the gas adsorption at −196 °C and 30 °C are not fully understood; they could rather be tentatively explained by the higher thermal motion and hence the flexibility and the accessibility of the windows at higher temperatures. Gas adsorption in the anhydride form would thus be favoured only when the temperature is high enough to allow sufficient flexibility at the pore windows. One may then suggest that, at such temperature, a

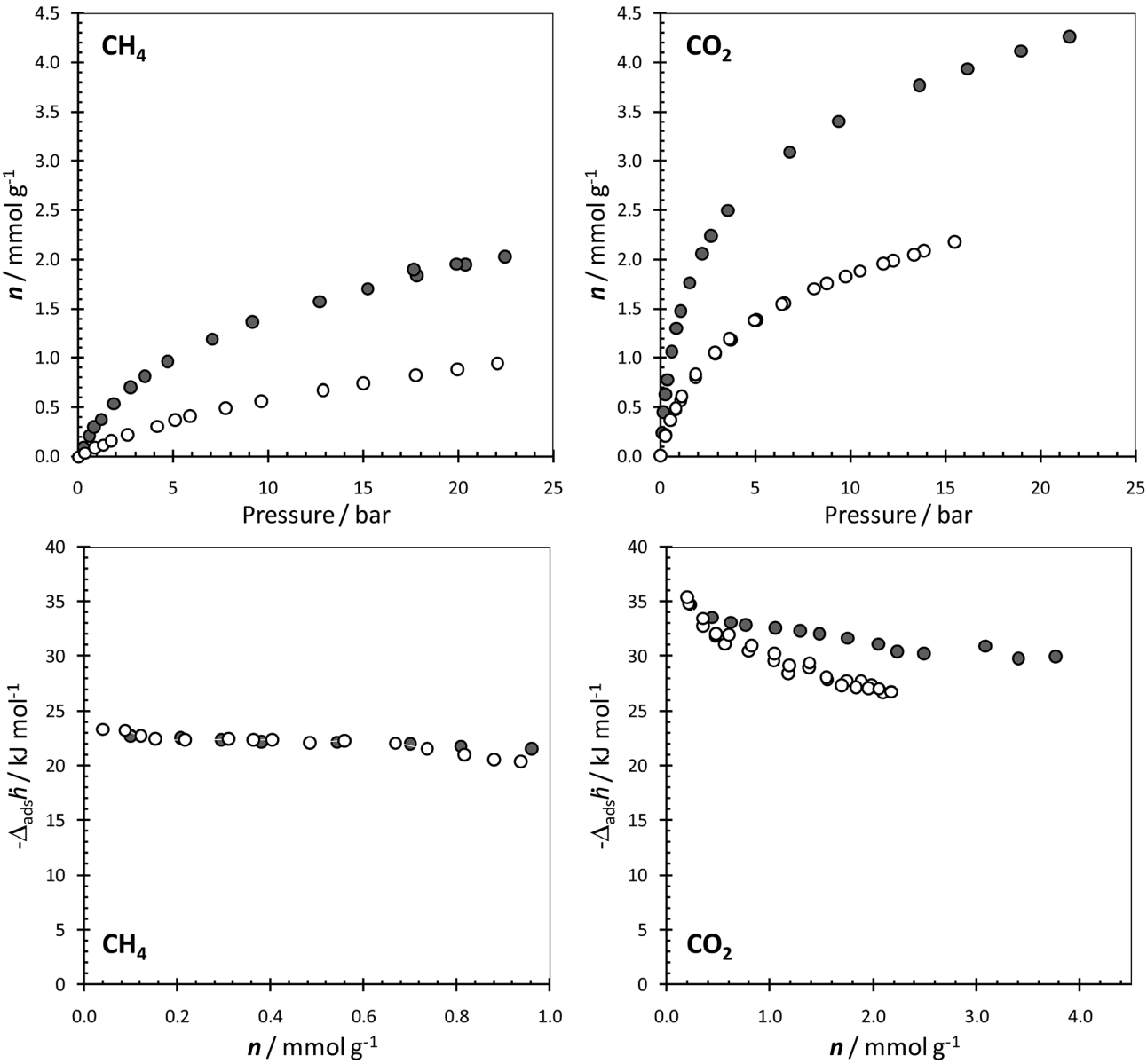

Fig. 11 Isotherms (upper curves) and adsorption enthalpies (lower curves) obtained at 30 °C with CH_4 (left) and CO_2 (right) for UiO-66(Zr)–$(COOH)_2$ outgassed to 30 °C (○) and 150 °C (●).

cooperative motion of the atoms at the pore mouth might be induced by the anhydride linkages, leading to higher capacities than without such linkages.

3.2.3 Reversibility of the anhydride formation. The dissociation of the anhydrides upon contact with water vapour was evidenced by different techniques. The PXRD patterns of the as-synthesized solids and after treatment at 180 °C and re-exposure to water were found to be almost identical (see ESI, Fig. S4†). Similarly, the ^{13}C CPMAS NMR spectra of both rehydrated solids are almost identical to those of the as-synthesized compounds, indicating that the process of formation of anhydrides is mostly reversible (Fig. 8).

IR spectroscopy showed that, after heating at 200 °C for 3 hours, anhydrides were formed as described above. Upon contact with water vapour, the anhydride IR bands were shifted to lower wavenumbers 1849 and 1781 cm^{-1} for the main bands of UiO-66(Zr)–(COOH) and 1857 and 1782 cm^{-1} for UiO-66(Zr)–$(COOH)_2$. The –COOH band in the presence of water was also shifted to 1708 cm^{-1} on UiO-66(Zr)–(COOH). Unfortunately, the very intense bands of the carboxylates tend to overwhelm this band on UiO-66(Zr)–$(COOH)_2$. Therefore a band at 1120 cm^{-1} was used instead to evaluate the carboxylic groups on this solid (specific experiments showed that the band at 1120 cm^{-1} on UiO-66(Zr)–$(COOH)_2$ evolved similar to the bands at 1740 cm^{-1}).

The band areas of anhydrides progressively decreased with contact time. Fig. 12 shows that both solids lose half of their anhydride content in less than 5 h. After a long exposure of both the solids to water (>20 h), *ca.* 40% of the anhydrides persisted on UiO-66(Zr)–(COOH) and *ca.* 20% on UiO-66(Zr)–$(COOH)_2$.

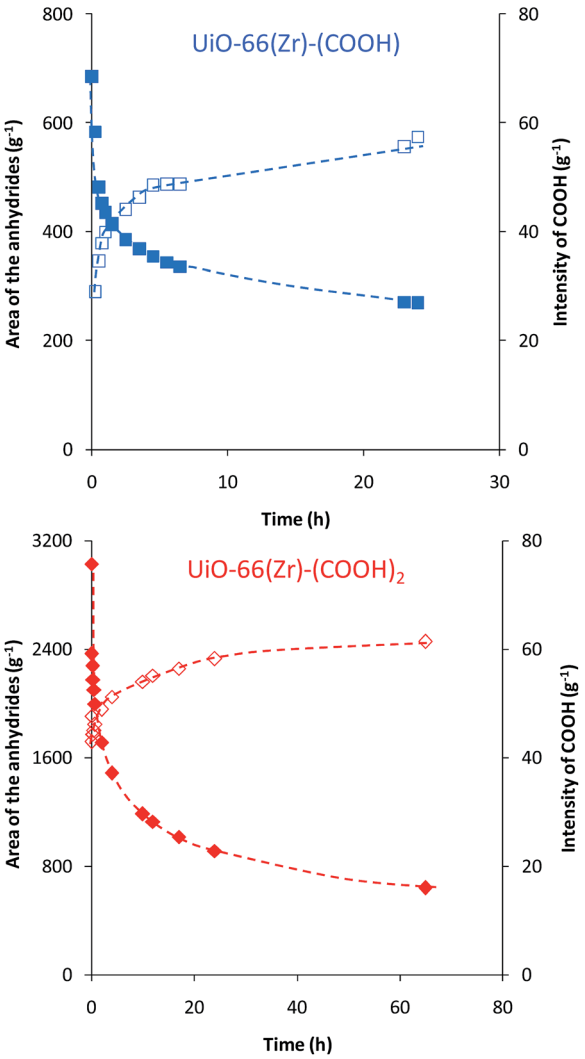

Fig. 12 Hydrolysis of the anhydrides on UiO-66(Zr)–(COOH) (top) and UiO-66(Zr)–$(COOH)_2$ (bottom). Evolution of the amount of anhydrides (solid symbols; area of the band at *ca.* 1860 cm^{-1}) and COOH groups (hollow symbols; intensity of the band) [note that for UiO-66(Zr)–(COOH), the COOH groups were estimated from the band at 1708 cm^{-1} while for UiO-66(Zr)–$(COOH)_2$ the intensity of the band at 1125 cm^{-1} was used instead].

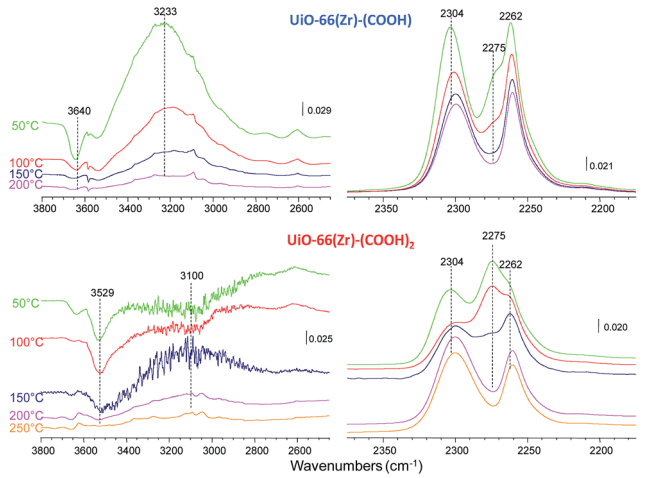

Fig. 13 FTIR spectra of UiO-66(Zr)–(COOH) (top) and UiO-66(Zr)–$(COOH)_2$ (bottom) after adsorption of CD_3CN on solids heated at various temperatures (the spectra shown are obtained after subtraction of the spectrum recorded before adsorption).

Meanwhile, bands due to carboxylic groups were partly restored.

This clearly supports the reversible formation of a large part of the anhydrides under the studied conditions. Moreover, the hydrolysis process appears independent of the type of functionalized solid.

3.3 Properties of the materials

3.3.1 Acidity. Acidity was evaluated by the adsorption of acetonitrile (CD_3CN) followed by FTIR (Fig. 13). In the solids evacuated at 50 °C, three ν(CN) vibration bands are observed at 2304, 2275 and 2262 cm^{-1} which can be attributed respectively to Lewis acid sites, Brønsted acid sites and physisorbed CD_3CN.[80] Lewis acid sites were also observed on the pristine UiO-66(Zr) by CO[40] or CD_3CN[44] adsorption. These bands appear associated with the dehydroxylation process of the inorganic cluster. However, although similar bands can be detected on the unmodified UiO-66(Zr) and on the UiO-66(Zr)–$(COOH)_x$ solids, differences are observed in the spectra.

After evacuation at 50 °C, Lewis acid sites appear on the carboxylic modified solids at a slightly higher wavenumber (2304 cm^{-1}) than on pure UiO-66(Zr) (2299 cm^{-1}) indicating a higher acid strength. However it shifts to 2299 cm^{-1} when the solid is activated at higher temperatures.

After evacuation at 50 °C, the band at 2275 cm^{-1} is only observed as a shoulder on UiO-66(Zr). This band is nevertheless much more intense with UiO-66(Zr)–(COOH) and even more prominent with UiO-66(Zr)–$(COOH)_2$, indicating a higher relative amount of Brønsted acid sites on the latter. Increasing the activation temperature did not change the position of this band but it disappeared progressively.

Brønsted acid sites observed after evacuation at mild temperature can originate from the μ_3-OH groups of the inorganic cluster. In the hydroxyl region on UiO-66(Zr), one can indeed observe on the difference spectrum (subtracted with the spectrum of the solid before adsorption), a negative band at 3672 cm^{-1} and a large perturbed positive band at 3460 cm^{-1}, which shifts to 3417 cm^{-1} when the physisorbed CD_3CN was removed. This shift, larger than the $\Delta\nu$(OH) = 180 cm^{-1} shift and expected for weakly H-bonded acetonitrile,[80] confirms that OH groups can act as Brønsted acid sites and give rise to the band at 2275 cm^{-1} on UiO-66(Zr). These μ_3-OH groups are also expected on UiO-66(Zr)–$(COOH)_x$ and thus probably also contribute to the Brønsted acid sites detected by acetonitrile. However, several features indicate substantial differences between UiO-66(Zr) and the UiO-66(Zr)–$(COOH)_x$ materials. First, the band intensity at 2275 cm^{-1} is higher on the UiO-66(Zr)–$(COOH)_x$ while a modification of the ligand is not expected to modify the inorganic cornerstone. Second, the

perturbation of the hydroxyl groups by CD_3CN is also different on the three solids. On UiO-66(Zr)–(COOH), the spectrum shows a main negative band at 3640 cm^{-1} and a positive band at 3233 cm^{-1}. This much larger shift ($\Delta\nu$(OH) = 410 cm^{-1}) is indicative of a higher overall acid strength and implies that the carboxylic groups also induce Brønsted acidity, stronger than the acidity of the pristine UiO-66(Zr). After evacuation at 100 °C, the shift is more important ($\Delta\nu$(OH) = 460 cm^{-1}). This higher strength is however not sufficient to be clearly evidenced by an additional shift of the ν(CN) band. It is therefore likely that the Brønsted acid sites detected are partly induced by the inorganic hydroxyl groups and partly by the organic carboxylic groups. On UiO-66(Zr)–$(COOH)_2$, the main negative band is observed at 3529 cm^{-1} but a positive band is not observed. In contrast, the solid evacuated at 50 °C shows a broad negative band of low intensity around 3100 cm^{-1}. The expected positive band due to perturbed μ_3-OH may be present but it is obscured by a larger negative band. Combination bands due to carboxylates are indeed expected in this region, which complicates the analysis. After activation at 100 and 150 °C, a positive broad band centred at 3100 cm^{-1} is finally obtained, while the formation of anhydrides has already suppressed the bonds between adjacent carboxylic groups. Bonds, likely the H-bonds between adjacent carboxylic groups, are thus probably displaced by CD_3CN. This band is at slightly lower wavenumber than for UiO-66(Zr)–(COOH), suggesting that this solid is more acidic.

Overall the band attributed to acetonitrile coordinated with Brønsted acid sites at 2275 cm^{-1} decreased on all the samples after evacuation of the solids at higher temperature (Fig. 14a). On UiO-66(Zr)–(COOH) and UiO-66(Zr)–$(COOH)_2$, Brønsted acid sites vanished in a similar manner. This decrease is consistent with both the dehydroxylation process and the fact that the number of carboxylic groups decreases upon heat treatment due to their transformation into anhydrides. The anhydride formation is thus detrimental to the overall amount of Brønsted acid sites.

Lewis acid sites detected by CD_3CN (Fig. 14b) evolved differently on UiO-66(Zr)–(COOH) and UiO-66(Zr)–$(COOH)_2$ but do not increase with the activation temperature as observed on UiO-66(Zr). This might indicate that dehydroxylation at low temperature is partially perturbed on the UiO-66(Zr)–$(COOH)_x$ solids, especially on UiO-66(Zr)–$(COOH)_2$ on which Lewis sites only increased above 150 °C. However, after activation at 200 °C, the concentration of Lewis acid sites was within the same range, around 300 μmol g^{-1}, very close to the values measured on unmodified UiO-66(Zr) or UiO-66(Zr)–(NH_2).

3.3.2 Conductivity. The values of the proton conductivity (σ_{dc}) of the hydrated UiO-66(Zr)–(COOH) and UiO-66(Zr)–$(COOH)_2$ solids are listed in Table 4 together with those of the hydrated UiO-66(Zr) and UiO-66(Zr)–NH_2 for comparison. The so-obtained values are much lower than those reported so far for the best proton conductor MOFs.[81] The samples can be classified as follows: σ_{dc} (UiO-66(Zr)–$(COOH)_2$) > σ_{dc} (UiO-66(Zr)–(COOH)) > σ_{dc} (UiO-66(Zr)) > σ_{dc} (UiO-66(Zr)–(NH_2)). A good correlation is observed between the increase of the proton conductivity and the expected acidity of the functional group, as previously reported for substituted MIL-53(M)s (M = Fe or Al),[22] which makes the most acidic UiO-66(Zr)–$(COOH)_2$ to associate with the highest conductivity. In the substituted UiO-66(Zr) series, the proton carriers are expected to originate from μ_3-OH groups constituting the metallic clusters and/or the functional groups linked to the organic ligands of the MOF. Considering that the number of the μ_3-OH groups is similar in the whole set of the modified UiO-66(Zr)s and that their acidity is neglected compared to the one exhibited by the protons of the functional groups,[22] one can conclude that the conductivity sequence is mainly governed by the Brønsted acidity of the substituted

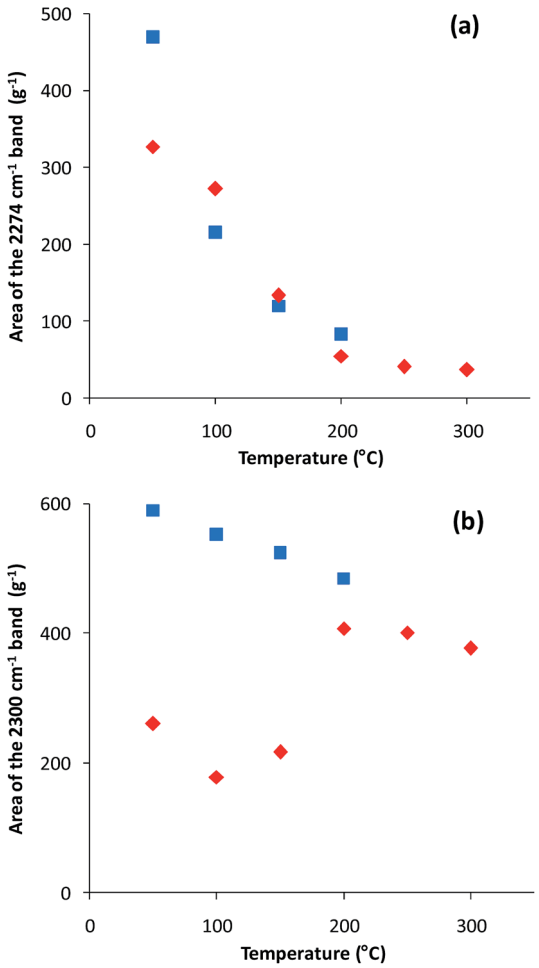

Fig. 14 Amount of Brønsted (a) and Lewis (b) acid sites detected by CD_3CN after heating at various temperatures of UiO-66(Zr)–(COOH) (■; blue) and UiO-66(Zr)–$(COOH)_2$ (◆; red).

Table 4 dc conductivity values of UiO-66(Zr)s and MIL-53(M)s, recorded at 25 °C in the hydrated state

	σ_{dc} (S cm^{-1})	
	MIL-53(M)s[22]	UiO-66(Zr)s
Non modified	2×10^{-8}	8×10^{-9}
–NH_2	2×10^{-9}	3×10^{-9}
–(COOH)	—	9×10^{-7}
–$(COOH)_2$	2×10^{-6}	5×10^{-6}

functional groups on the ligands. Both absolute values and trend agree very well with those previously reported for the analogous functionalized MIL-53(M)s (M = Fe or Al)[22] This suggests that both types of materials are characterized by a similar ordered array of the water molecules, which ensures the pathway for the proton propagation.[82,83] Finally, we also studied the conductivity properties of the UiO-66(Zr)–(COOH) and UiO-66(Zr)–$(COOH)_2$ solids *in situ* treated at 150 °C under nitrogen flow for 4 hours. No dc conductivity was detected in the temperature range studied [20–150 °C], although in the absence of water a signal should appear, as the characteristic distances between the functions bearing the proton carriers ~2.9 Å (see the DFT optimized structures of UiO-66(Zr)–(COOH) and UiO-66(Zr)–$(COOH)_2$) are expected to make possible the propagation of the protons. The absence of dc conductivity is indeed consistent with the loss of acidic protons which occurs concomitantly with the formation of anhydride bridges.

4. Conclusion

The impact of free pending carboxylic side-groups on MOF structures has been tested in the case of UiO-66(Zr)'s. UiO-66(Zr)–(COOH) and UiO-66(Zr)–$(COOH)_2$ have been synthesized directly from trimellitic and pyromellitic acids using an environmentally friendly water-based synthesis route. After a detailed high throughput and kinetic study of their crystallization process, the robustness of their synthesis was established, allowing their efficient up-scaling. The introduction of free carboxylic acid groups on the organic linker induced modifications of the pristine UiO-66(Zr), which, for both solids, led to an enhanced Brønsted acidity and proton conductivity, due to the sufficient mobility of the acidic protons of the free carboxylic groups. These acid groups also have the ability to act as intra-framework cross-linking centres *via* the formation of anhydride species across the pores without neither structure degradation nor decrease of their gas sorption properties at ambient temperature. However, dehydration of the functional carboxylic groups led to a detrimental effect on the acidity and conductivity. Nonetheless, carboxylic groups could easily and reversibly be restored upon contact with water vapour. These features confirm on the whole that functionalisation of MOFs with free carboxylic acid groups is thus an efficient and versatile method for several types of applications.

Acknowledgements

The authors acknowledge the financial support of the European Community within the Seventh Framework Programme (FP7/2007-2013) under grant agreement no. 228862 (Project MACADEMIA). Parts of this research were carried out at the light source F3 at DESY, a member of the Helmholtz Association (HGF). G. Le Bars is thanked for performing IR measurements, C. Sicard for providing a batch of UiO-66(Zr)–COOH, N. Stock for providing the HT synthesis experimental setup, and S. El Ghazi for her participation in the conductivity measurements. G. M. thanks the Institut Universitaire de France for its support.

Notes and references

1 M. Eddaoudi, J. Kim, N. Rosi, D. Vodak, J. Wachter, M. O'Keeffe and O. M. Yaghi, *Science*, 2002, **295**, 469.
2 T. Devic, P. Horcajada, C. Serre, F. Salles, G. Maurin, B. Moulin, D. Heurtaux, G. Clet, A. Vimont, J.-M. Grenèche, B. L. Ouay, F. Moreau, E. Magnier, Y. Filinchuk, J. Marrot, J.-C. Lavalley, M. Daturi and G. Férey, *J. Am. Chem. Soc.*, 2010, **132**, 1127.
3 M. Kandiah, M. H. Nilsen, S. Usseglio, S. Jakobsen, U. Olsbye, M. Tilset, C. Larabi, E. A. Quadrelli, F. Bonino and K. P. Lillerud, *Chem. Mater.*, 2010, **22**, 6632.
4 H. Deng, C. J. Doonan, H. Furukawa, R. B. Ferreira, J. Towne, C. B. Knobler, B. Wang and O. M. Yaghi, *Science*, 2010, **327**, 846.
5 P. Horcajada, F. Salles, S. Wuttke, T. Devic, D. Heurtaux, G. Maurin, A. Vimont, M. Daturi, O. David, E. Magnier, N. Stock, Y. Filinchuk, D. Popov, C. Riekel, G. Férey and C. Serre, *J. Am. Chem. Soc.*, 2011, **133**, 17839.
6 S. Biswas, T. Ahnfeldt and N. Stock, *Inorg. Chem.*, 2011, **50**, 9518.
7 S. Henke, A. Schneemann, A. Wütscher and R. A. Fischer, *J. Am. Chem. Soc.*, 2012, **134**, 9464.
8 S. M. Cohen, *Chem. Rev.*, 2012, **112**, 970.
9 G. Akiyama, R. Matsuda, H. Sato, M. Takata and S. Kitagawa, *Adv. Mater.*, 2011, **23**, 3294.
10 M. Lin Foo, S. Horike, T. Fukushima, Y. Hijikata, Y. Kubota, M. Takata and S. Kitagawa, *Dalton Trans.*, 2012, **41**, 13791.
11 M. G. Goesten, J. Juan-Alcañiz, E. V. Ramos-Fernandez, K. B. Sai Sankar Gupta, E. Stavitski, H. van Bekkum, J. Gascon and F. Kapteijn, *J. Catal.*, 2011, **281**, 177.
12 S. Biswas, J. Zhang, Z. Li, Y.-Y. Liu, M. Grzywa, L. Sun, D. Volkmer and P. Van Der Voort, *Dalton Trans.*, 2013, **42**, 4730.
13 T. Devic, F. Salles, S. Bourrelly, B. Moulin, G. Maurin, P. Horcajada, C. Serre, A. Vimont, J.-C. Lavalley, H. Leclerc, G. Clet, M. Daturi, P. L. Llewellyn, Y. Filinchuk and G. Férey, *J. Mater. Chem.*, 2012, **22**, 10266.
14 N. Reimer, B. Gil, B. Marszalek and N. Stock, *CrystEngComm*, 2012, **14**, 4119.
15 J. F. Eubank, H. Mouttaki, A. J. Cairns, Y. Belmabkhout, L. Wojtas, R. Luebke, M. Alkordi and M. Eddaoudi, *J. Am. Chem. Soc.*, 2011, **133**, 14204.
16 V. Guillerm, D. Kim, J. F. Eubank, R. Luebke, X. Liu, K. Adil, M. S. Lah and M. Eddaoudi, *Chem. Soc. Rev.*, 2014, **43**, 6141.
17 J. Juan-Alcaniz, R. Gielisse, A. B. Lago, E. V. Ramos-Fernandez, P. Serra-Crespo, T. Devic, N. Guillou, C. Serre, F. Kapteijn and J. Gascon, *Catal. Sci. Technol.*, 2013, **3**, 2311.
18 A. Torrisi, C. Mellot-Draznieks and R. G. Bell, *J. Chem. Phys.*, 2010, **132**, 044705.
19 Q. Yang, A. D. Wiersum, P. L. Llewellyn, V. Guillerm, C. Serre and G. Maurin, *Chem. Commun.*, 2011, **47**, 9603.
20 Z. Xiang, S. Leng and D. Cao, *J. Phys. Chem. C*, 2012, **116**, 10573.
21 A. Morozan and F. Jaouen, *Energy Environ. Sci.*, 2012, **5**, 9269.

22 A. Shigematsu, T. Yamada and H. Kitagawa, *J. Am. Chem. Soc.*, 2011, **133**, 2034.
23 C. A. Allen, J. A. Boissonnault, J. Cirera, R. Gulland, F. Paesani and S. M. Cohen, *Chem. Commun.*, 2013, **49**, 3200.
24 G. Distefano, H. Suzuki, M. Tsujimoto, S. Isoda, S. Bracco, A. Comotti, P. Sozzani, T. Uemura and S. Kitagawa, *Nat. Chem.*, 2013, **5**, 335.
25 Y. Luo, K. Bernot, G. Calvez, S. Freslon, C. Daiguebonne, O. Guillou, N. Kerbellec and T. Roisnel, *CrystEngComm*, 2013, **15**, 1882.
26 H.-L. Jiang, D. Feng, T.-F. Liu, J.-R. Li and H.-C. Zhou, *J. Am. Chem. Soc.*, 2012, **134**, 14690.
27 J. H. Cavka, S. Jakobsen, U. Olsbye, N. Guillou, C. Lamberti, S. Bordiga and K. P. Lillerud, *J. Am. Chem. Soc.*, 2008, **130**, 13850.
28 S. J. Garibay and S. M. Cohen, *Chem. Commun.*, 2010, **46**, 7700.
29 M. Kim and S. M. Cohen, *CrystEngComm*, 2012, **14**, 4096.
30 H. Jasuja, J. Zang, D. S. Sholl and K. S. Walton, *J. Phys. Chem. C*, 2012, **116**, 23526.
31 S. Biswas and P. Van Der Voort, *Eur. J. Inorg. Chem.*, 2013, 2154.
32 Q. Yang, S. Vaesen, F. Ragon, A. D. Wiersum, D. Wu, A. Lago, T. Devic, C. Martineau, F. Taulelle, P. L. Llewellyn, H. Jobic, C. Zhong, C. Serre, G. De Weireld and G. Maurin, *Angew. Chem., Int. Ed.*, 2013, **52**, 10316.
33 V. Guillerm, F. Ragon, M. Dan-Hardi, T. Devic, M. Vishnuvarthan, B. Campo, A. Vimont, G. Clet, Q. Yang, G. Maurin, G. Férey, A. Vittadini, S. Gross and C. Serre, *Angew. Chem., Int. Ed.*, 2012, **51**, 9267.
34 D. Feng, Z.-Y. Gu, J.-R. Li, H.-L. Jiang, Z. Wei and H.-C. Zhou, *Angew. Chem., Int. Ed.*, 2012, **51**, 10307.
35 W. Morris, B. Volosskiy, S. Demir, F. Gándara, P. L. McGrier, H. Furukawa, D. Cascio, J. F. Stoddart and O. M. Yaghi, *Inorg. Chem.*, 2012, **51**, 6443.
36 J. E. Mondloch, W. Bury, D. Fairen-Jimenez, S. Kwon, E. J. DeMarco, M. H. Weston, A. A. Sarjeant, S. T. Nguyen, P. C. Stair, R. Q. Snurr, O. K. Farha and J. T. Hupp, *J. Am. Chem. Soc.*, 2013, **135**, 10294.
37 D. Feng, H.-L. Jiang, Y.-P. Chen, Z.-Y. Gu, Z. Wei and H.-C. Zhou, *Inorg. Chem.*, 2013, **52**, 12661.
38 V. Bon, I. Senkovska, I. A. Baburin and S. Kaskel, *Cryst. Growth Des.*, 2013, **13**, 1231.
39 V. Bon, I. Senkovska, M. S. Weiss and S. Kaskel, *CrystEngComm*, 2013, **15**, 9572.
40 A. D. Wiersum, E. Soubeyrand-Lenoir, Q. Yang, B. Moulin, V. Guillerm, M. B. Yahia, S. Bourrelly, A. Vimont, S. Miller, C. Vagner, M. Daturi, G. Clet, C. Serre, G. Maurin and P. L. Llewellyn, *Chem.–Asian J.*, 2011, **6**, 3270.
41 L. Valenzano, B. Civalleri, S. Chavan, S. Bordiga, M. H. Nilsen, S. Jakobsen, K. P. Lillerud and C. Lamberti, *Chem. Mater.*, 2011, **23**, 1700.
42 S. Chavan, J. G. Vitillo, D. Gianolio, O. Zavorotynska, B. Civalleri, S. Jakobsen, M. H. Nilsen, L. Valenzano, C. Lamberti, K. P. Lillerud and S. Bordiga, *Phys. Chem. Chem. Phys.*, 2012, **14**, 1614.
43 T. Duerinck, R. Bueno-Perez, F. Vermoortele, D. E. De Vos, S. Calero, G. V. Baron and J. F. M. Denayer, *J. Phys. Chem. C*, 2013, **117**, 12567.
44 F. Vermoortele, B. Bueken, G. Le Bars, B. Van de Voorde, M. Vandichel, K. Houthoofd, A. Vimont, M. Daturi, M. Waroquier, V. Van Speybroeck, C. Kirschhock and D. E. De Vos, *J. Am. Chem. Soc.*, 2013, **135**, 11465.
45 D. Wu, G. Maurin, Q. Yang, C. Serre, H. Jobic and C. Zhong, *J. Mater. Chem. A*, 2014, **2**, 1657.
46 N. Stock, *Microporous Mesoporous Mater.*, 2010, **129**, 287.
47 L. Engelke, M. Schaefer, M. Schur and W. Bensch, *Chem. Mater.*, 2001, **13**, 1383.
48 A. Boultif and D. Louër, *J. Appl. Crystallogr.*, 2004, **37**, 724.
49 T. Roisnel and J. Rodriguez-Carvajal, in *Epdic 7: European Powder Diffraction, Pts 1 and 2*, ed. R. Delhez and E. J. Mittemeijer, Trans Tech Publications Ltd, Zurich-Uetikon, 2001, p. 118.
50 B. M. Fung, A. K. Khitrin and K. Ermolaev, *J. Magn. Reson.*, 2000, **142**, 97.
51 D. Massiot, F. Fayon, M. Capron, I. King, S. Le Calvé, B. Alonso, J.-O. Durand, B. Bujoli, Z. Gan and G. Hoatson, *Magn. Reson. Chem.*, 2002, **40**, 70.
52 T. Düren, F. Millange, G. Férey, K. S. Walton and R. Q. Snurr, *J. Phys. Chem. C*, 2007, **111**, 15350.
53 A. L. Myers and P. A. Monson, *Langmuir*, 2002, **18**, 10261.
54 M. D. Segall, J. D. L. Philip, M. J. Probert, C. J. Pickard, P. J. Hasnip, S. J. Clark and M. C. Payne, *J. Phys.: Condens. Matter*, 2002, **14**, 2717.
55 S. J. Clark, M. D. Segall, C. J. Pickard, P. J. Hasnip, M. J. Probert, K. Refson and M. C. Payne, *Z. Kristallogr.*, 2005, **220**, 567.
56 J. P. Perdew, K. Burke and M. Ernzerhof, *Phys. Rev. Lett.*, 1996, **77**, 3865.
57 J. R. Yates, C. J. Pickard and F. Mauri, *Phys. Rev. B: Condens. Matter Mater. Phys.*, 2007, **76**, 024401.
58 A. D. Wiersum, C. Giovannangeli, D. Vincent, E. Bloch, H. Reinsch, N. Stock, J. S. Lee, J.-S. Chang and P. L. Llewellyn, *ACS Comb. Sci.*, 2013, **15**, 111.
59 P. L. Llewellyn and G. Maurin, *C. R. Chim.*, 2005, **8**, 283.
60 A. Schaate, P. Roy, A. Godt, J. Lippke, F. Waltz, M. Wiebcke and P. Behrens, *Chem.–Eur. J.*, 2011, **17**, 6643.
61 F. Ragon, P. Horcajada, H. Chevreau, Y. K. Hwang, U. H. Lee, S. R. Miller, T. Devic, J.-S. Chang and C. Serre, *Inorg. Chem.*, 2014, **53**, 2491.
62 V. Bon, V. Senkovskyy, I. Senkovska and S. Kaskel, *Chem. Commun.*, 2012, **48**, 8407.
63 M. J. Katz, Z. J. Brown, Y. J. Colon, P. W. Siu, K. A. Scheidt, R. Q. Snurr, J. T. Hupp and O. K. Farha, *Chem. Commun.*, 2013, **49**, 9449.
64 L. Pan, R. Heddy, J. Li, C. Zheng, X.-Y. Huang, X. Tang and L. Kilpatrick, *Inorg. Chem.*, 2008, **47**, 5537.
65 I. Pappas, M. Fitzgerald, X.-Y. Huang, J. Li and L. Pan, *Cryst. Growth Des.*, 2009, **9**, 5213.
66 F. Ragon, P. Horcajada, H. Chevreau, T. Devic and C. Serre, 2014, in preparation.
67 A. Apelblat, E. Manzurola and N. Abo Balal, *J. Chem. Thermodyn.*, 2006, **38**, 565.

68 M. Avrami, *J. Chem. Phys.*, 1941, **9**, 177.
69 B. V. Erofe'ev, *C. R. (Dokl.) Acad. Sci. URSS*, 1946, **52**, 511.
70 A. F. Gualtieri, *Phys. Chem. Miner.*, 2001, **28**, 719.
71 J. D. Hancock and J. H. Sharp, *J. Am. Ceram. Soc.*, 1972, **55**, 74.
72 F. Millange, R. I. Walton and D. O'Hare, *J. Mater. Chem.*, 2000, **10**, 1713.
73 N. Pienack, C. Näther and W. Bensch, *Eur. J. Inorg. Chem.*, 2009, 937.
74 H. Reinsch and N. Stock, *CrystEngComm*, 2013, **15**, 544.
75 F. Millange, R. El Osta, M. E. Medina and R. I. Walton, *CrystEngComm*, 2011, **13**, 103.
76 G. C. Shearer, S. Chavan, J. Ethiraj, J. G. Vitillo, S. Svelle, U. Olsbye, C. Lamberti, S. Bordiga and K. P. Lillerud, *Chem. Mater.*, 2014, **26**, 4068.
77 F. González-Sánchez, *Spectrochim. Acta*, 1958, **12**, 17.
78 W. Dauben and W. Epstein, *J. Org. Chem.*, 1959, **24**, 1595.
79 S. Devautour-Vinot, G. Maurin, C. Serre, P. Horcajada, D. Paula da Cunha, V. Guillerm, E. de Souza Costa, F. Taulelle and C. Martineau, *Chem. Mater.*, 2012, **24**, 2168.
80 C. Morterra, G. Cerrato, E. Novarino and M. P. Mentruit, *Langmuir*, 2003, **19**, 5708.
81 P. Ramaswamy, N. E. Wong and G. K. H. Shimizu, *Chem. Soc. Rev.*, 2014, **43**, 5913.
82 P. Colomban, *Proton Conductors: Solids, Membranes and Gels-materials and Devices*, Cambridge University Press, Cambridge (UK), 1992.
83 A. Planchais, S. Devautour-Vinot, F. Salles, F. Ragon, T. Devic, C. Serre and G. Maurin, *J. Phys. Chem. C*, 2014, **118**, 14441.